

Relationship between cavitation structures and cavitation damage

Matevž Dular^{a,*}, Bernd Bachert^a, Bernd Stoffel^a, Brane Širok^b

^a Chair of Turbomachinery and Fluid Power, Darmstadt University of Technology, Magdalenenstr. 4, 64289 Darmstadt, Germany

^b Laboratory for Water Turbine Machines, University of Ljubljana, Askerceva 6, 1000 Ljubljana, Slovenia

Received 6 February 2004; received in revised form 9 August 2004; accepted 12 August 2004

Available online 1 October 2004

Abstract

A study of visual and erosion effects of cavitation on simple single hydrofoil configurations in a cavitation tunnel was made. A two-dimensional hydrofoil with circular leading edge was used for the experiments. In addition, the hydrofoil geometry was modified to obtain some three-dimensional cavitation effects. A thin copper foil, applied to the surface of the hydrofoil, was used as an erosion sensor. Cavitation phenomenon above hydrofoils at different flow conditions (system pressure, water gas content) was observed. Images of vapour cavities from above and from side view were taken. A statistical evaluation of cavitation structures was made. Images of damaged copper coated hydrofoil surface were taken under sufficient magnification. A pit-count method, based on computer-aided image processing, was used for direct measurement of the cavitation erosion by evaluating the damage of the surface of the hydrofoil. A relation between characteristics of cavitation structures and cavitation damage was established.

© 2004 Elsevier B.V. All rights reserved.

Keywords: Cavitation; Damage; Computer-aided image processing; Single hydrofoil; Pit-count method

1. Introduction

Cavitation phenomenon, characterised by vapour generation and condensation, occurs frequently in hydraulic machines. It causes vibration, increase of hydrodynamic drag, changes in the flow hydrodynamics, noise, thermal and light effects like luminescence and, the most important of all, cavitation erosion.

It was Rayleigh [1] who first introduced the problem of cavitation erosion of the ship propellers. Since then, a wide range of studies that deal with problems from bubble dynamics to material testing, have been made.

It is recognised that the most common mechanism of cavitation erosion is the so-called micro-jet phenomenon [2]. Benjamin and Ellis [3] provided experimental proof of micro-jet formation. The process was later theoretically approached

by Plesset and Chapmann [4] and again experimentally confirmed by Lauterborn and Bolle [5] who provided high-speed photographic observations of the initial stages of the collapse of a laser-generated bubble near the wall. It was found that the liquid jet that penetrates the bubble can reach a velocity of several 100 m/s. Bourne and Field [6] observed the interactions of plane shock waves with single cavities and studied the processes occurring within the cavity during collapse.

There is some evidence that other mechanisms are to be considered as important as the micro-jet phenomenon for the cavitation damage occurrence. Mørch [7] reports of the shock waves generated at the collapse of bubble clusters, while Tong et al. [8] considers also the splashing effect which follows the impact of the liquid jet.

Recently, there were many attempts to predict and control the cavitation erosion. Some ideas can be found in PhD works of Böhm [9], Hofmann [10] and Lohrberg [11].

Fig. 1 schematically shows the process of cavitation cloud implosion that begins with its separation from the attached part of cavitation. It then travels with the flow and collapses in the higher pressure region. Its collapse causes the formation of the re-entrant jet (frame 4), which causes a new

* Corresponding author. Tel.: +49 6151 2753; fax: +49 6151 2453.

E-mail addresses: dular@tfa.maschinenbau.tu-darmstadt.de, matevz.dular@email.si (M. Dular), bbachert@tfa.maschinenbau.tu-darmstadt.de, bernd.bachert@bfw.srh.de (B. Bachert), stoffel@tfa.maschinenbau.tu-darmstadt.de (B. Stoffel), brane.sirok@fs.uni-lj.si (B. Širok).

Nomenclature

A	pixel gray level
i	i co-ordinate in the image
j	j co-ordinate in the image
n	image number
N	number of images
p_∞	pressure at the inlet to the test section
p_v	vapour pressure
Re	Reynolds number ($=vd/\nu$)
T_∞	fluid temperature
v	velocity

Greek letters

μ	mean value of gray level
ν	viscosity
σ	cavitation number
σ	standard deviation of gray level

separation of the cavitation cloud. Frame 6 shows the possibility of micro-jet formation (the inserted image is courtesy of Prof. L.A. Crum published in [2]).

Because of the collapse of a group of bubbles (cavitation cloud), a pressure wave of magnitude of several 100 kPa is emitted. These repeating transient collapses can cause cavitation erosion and can also produce some other effects like luminescence [12]. The pressure wave with sufficient magnitude, acts on the bubbles of a spherical shape that are positioned close to the surface of the submerged body. The shape of the bubble becomes unstable, it begins to oscillate. If the amplitude of oscillations is big enough, a micro-jet phenomenon can occur. The fluid that surrounds the bubble takes a shape of jet through the bubble in the direction towards the solid surface (Fig. 2).

This micro-jet can reach high local velocities (several 100 m/s) that cause a shock (the order of magnitude is bigger than 1 GPa, the duration is approximately 1 ns and the affected area is in order of a few μm^2) with high local tension of the material [13]. The damage of the surface appears

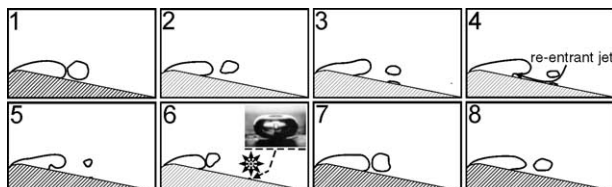


Fig. 1. Collapse of the united group of bubbles (cavitation cloud). The process begins with cavitation cloud separation, which is caused by the re-entrant jet (4). The cavitation cloud travels with the flow and collapses in a higher pressure region. The shock wave emitted at cavitation cloud collapse influences the bubbles that are positioned near the wall, which can respond with the formation of a micro-jet (inserted frame is courtesy of Prof. L.A. Crum published in [2]). The collapse of the cloud generates the re-entrant jet that causes a new cavitation cloud separation and the process is repeated.

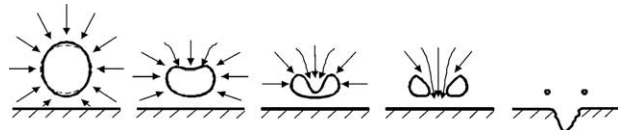


Fig. 2. Micro-jet mechanism. As a response to the pressure wave the initially spherical bubble starts to oscillate. If the oscillations are big enough the surrounding liquid penetrates the bubble and flows through it toward the solid surface. As it hits the solid surface a formation of a pit (plastic deformation) can occur.

in a form of microscopic plastic deformations, called pits [14].

Due to difficulties of measuring the pressure peaks caused by bubble implosions it is not possible to define the aggressiveness of cavitation erosion on purely hydrodynamic basis. Methods of measuring are, for example vibratory determination [15] or the usage of soft metal (aluminium or copper) or paint coating of the submerged body as a sensor [16–20]. The erosion evaluation method, using the number, distribution and shape of the pits caused by bubble implosions on the soft surface coating gives us a detailed knowledge of the cavitation erosion mechanism.

Different approaches of cavitation erosion prediction and its relation to macroscopic cavitation structures have already been discussed [21–24].

This paper discusses the relation between optically observed cavitation structures above different single hydrofoils and the erosion on the surface of the hydrofoils. Due to the time limitation of the experiment a soft copper foil was applied to the surface of the hydrofoil to obtain the sufficient number of pits in a shorter time period (30 min to 4 h). To obtain a three-dimensional cavitation pattern and asymmetric erosion distribution a basic (symmetric two-dimensional) hydrofoil configuration was modified by sweeping back the leading edge at a certain angle (Fig. 3).

Cavitation was studied on three different hydrofoils at different operating conditions (cavitation number, water gas content).

The final goal of the work is to find general correlations and rules, which will serve as a base for development of an expert system for monitoring and control of cavitation

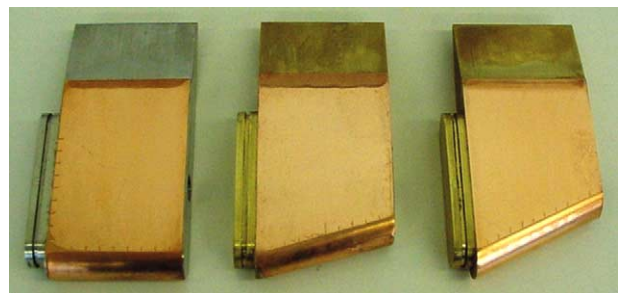


Fig. 3. Copper coated CLE, ALE15 and ALE25 hydrofoils used for the experiment. The hydrofoils are 107.9 mm long, 50 mm wide and 16 mm thick. To get some three-dimensional cavitation effects, the basic geometry was modified by sweeping back the leading edge for 15° and 25°.

in hydraulic machinery by means of different visualization techniques.

2. Experimental set up

Cavitation tests were performed in a cavitation tunnel at the Laboratory for Turbomachinery and Fluid power, Darmstadt University of Technology.

Three simple hydrofoils were used. The basic geometry is 50 mm wide, 107.9 mm long and 16 mm thick symmetric hydrofoil with circular leading edge and parallel walls (CLE: Circular Leading Edge hydrofoil). In order to obtain three-dimensional cavitation effects, the basic geometry was modified by sweeping back the leading edge at an angle of 15° and 25° , respectively (ALE15 and ALE25; ALE: Asymmetric Leading Edge hydrofoil; Fig. 3).

Hydrofoil was put into a rectangular test section of the cavitation tunnel (Fig. 4) with closed circuit what enabled to vary the system pressure and consequently the cavitation number. The test section of the cavitation tunnel is 500 mm long, 100 mm high and 50 mm wide. Two observation windows are mounted for top and side view observation.

The velocity in the reference plane upstream of the hydrofoil was held constant at 13 m/s (Reynolds number based on hydrofoil thickness was: $Re = 208,000$). Developed cavitating flow was observed at 5° incidence angle and at different values of cavitation number (2.5, 2.3, 2.0), which is defined as the difference between the pressure at the inlet to the test section p_∞ (measured on the position 400 mm upstream of the hydrofoil) and vapour pressure p_v (at system temperature T_∞) divided by the dynamic pressure (defined by fluid density ρ and flow velocity v):

$$\sigma = \frac{p_\infty - p_v T_\infty}{\rho v^2 / 2}. \quad (1)$$

Decreasing the cavitation number, results in higher probability in cavitation occurrence or in increase of the magnitude of the already present cavitation.

Considering the combination of inaccuracies of pressure, velocity and temperature measurements, the cavitation number could be determined within ± 0.02 of global uncertainty.

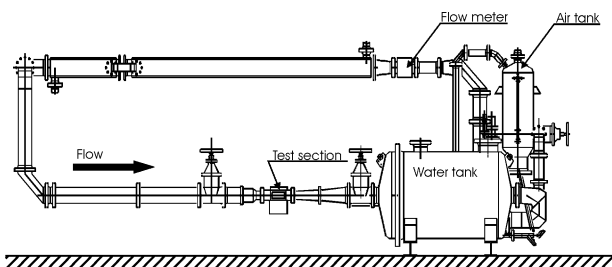


Fig. 4. Cavitation tunnel. The test section is 500 mm long 100 mm high and 50 mm wide. The maximal flow velocity is 20 m/s. The pressure at the inlet to the test section can be adjusted between 0.2 and 5 bar.

Table 1
Parameters of investigated cavitation conditions

Test	Hydrofoil	Cavitation number	Gas content (mg/l _w)
1	CLE	2.0	14.0
2	CLE	2.3	13.8
3	CLE	2.5	14.0
4	CLE	2.0	47.8
5	CLE	2.3	48.9
6	CLE	2.5	49.2
7	ALE15	2.0	14.8
8	ALE15	2.3	14.5
9	ALE15	2.5	14.9
10	ALE25	2.0	14.8
11	ALE25	2.3	14.7
12	ALE25	2.5	14.7

Water quality, which can be measured by its content of dissolved and undissolved gasses, was changed using the bubble generator system in the range from 14.3 ± 0.5 mg_g/l_w (milligrams of gas per liter of water) for low gas content to 48.5 ± 0.7 mg_g/l_w for high gas content.

The parameters of the experiments can be found in Table 1.

3. Cavitation image capturing

A sufficient number of images of vapour cavities from top and side view were taken in order to get a representative pattern for each cavitation condition (Figs. 5 and 9).

A CCD camera SensiCam with sensor CCD-Interline Progressive Scan was used. Images were captured at 8 bit resolution in m-jpeg format. The size of captured image is 860×1280 pixels for the top view and 1280×860 pixels in case of the side view.

The illumination was provided by stroboscopic light. The position of the light source and the CCD camera can be seen in Fig. 5. Frequency of image capturing was relatively low, approximately 2 Hz.

Fig. 6 shows a sequence of six images of cavitation structures on ALE25 hydrofoil at low gas content and at a cavitation number of 2.0 from top view. A significant dynamic cavitation behaviour can be seen near the front wall

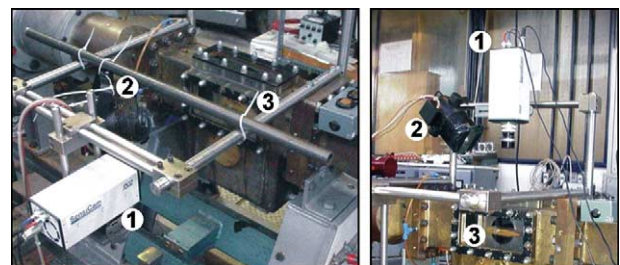


Fig. 5. The arrangement of CCD camera (1), stroboscopic light (2) and hydrofoil (3) for a side (left picture) and top view (right picture) image acquisition. It was found that the light source must be positioned at 45° to the camera to get the best image quality.

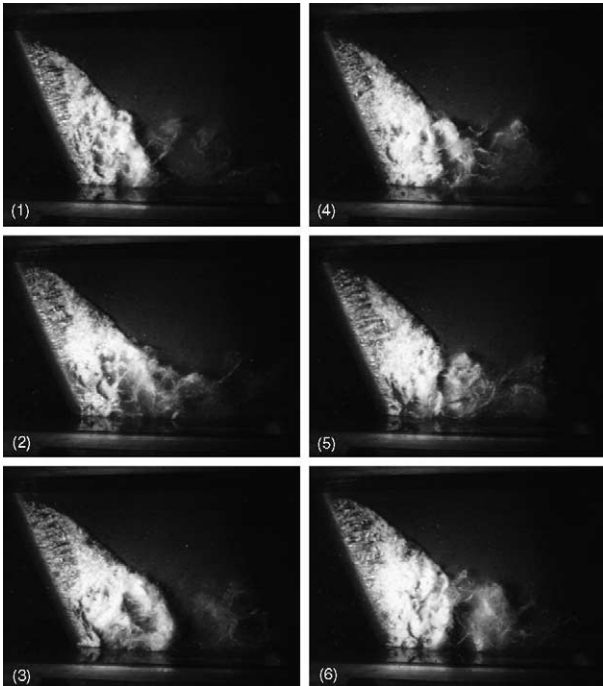


Fig. 6. Sequence of top view images for ALE25 hydrofoil. The flow is from left to the right. Significant dynamic cavitation behaviour can be seen near the front wall, while the cavitation at the rear wall remains nearly steady.

(fluctuations of cavitation region with separation of the cavitation cloud) while cavitation at the rear wall (where the hydrofoil length is the greatest) remains nearly steady (with no cloud separation).

4. Cavitation erosion tests

Due to the problems with reproducibility of the galvanic copper coating method, only a small part of the surface was investigated for the cavitation erosion in previous investigations. This was done using pure copper specimens inserted into the hydrofoil [10]. To get the information about the erosion on the whole surface of the hydrofoil, a polished copper foil, 0.2-mm thick, was fixed to its surface using adhesive film. The hardness of the copper coating was approximately 40 HV. A sufficient number of pits was obtained after 1 h exposure to the cavitating flow (the exposure time was constant for all operating conditions).

Pits have a diameter of magnitude order 10^{-5} m, and can be distinguished only by sufficient magnification. Images of the pitted surface were acquired using an Olympus BX-40 microscope and a CCD camera (Fig. 7).

The enlargement scale was 50:1 leading to the resolution of $1.95 \mu\text{m}$ per pixel. 925 images (one image embraces an area of $1.2 \text{ mm} \times 1.5 \text{ mm}$ big) of the pitted surface were taken for each operating point (the part of the surface evaluated by images represents approximately 48% of the copper coated hydrofoil surface).

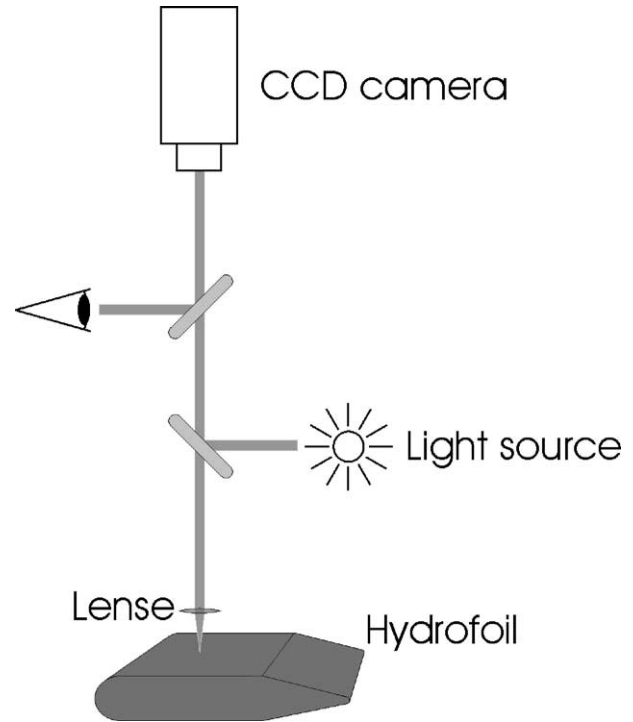


Fig. 7. Camera, microscope, light source and hydrofoil arrangement for surface image acquisition. About 925 images of the pitted surface were taken for each experiment.

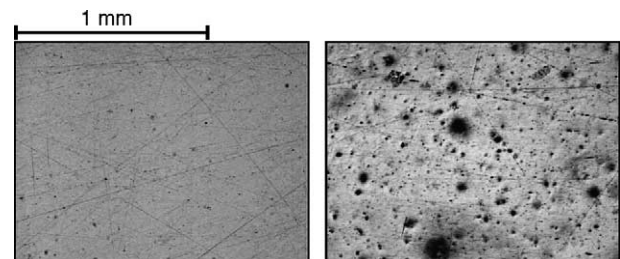


Fig. 8. Image of the surface prior (left) and after (right) the exposure to the cavitating flow. While we see no damage on the left image, almost 5% of the surface on the right image is covered with pits.

Fig. 8 shows an image of the surface before the exposure to cavitating flow (left) (0% damaged surface) and after 1 h of exposure (right) (4.98% damaged surface).

5. Image post-processing

Image post-processing is based on the fact that image n with ij pixels can be presented as a matrix with ij elements. 8 bit resolution gives 256 levels of grey level $A(i, j, n)$, which the matrix element can occupy (0 for black pixel and 255 for white pixel):

$$A(i, j, n) \in \{0, 1, \dots, 255\}. \quad (2)$$

Each image is presented as a matrix:

$$\text{Image}(n) = \begin{pmatrix} A(1, 1, n) & \cdots & A(i, 1, n) \\ A(1, 2, n) & \cdots & A(i, 2, n) \\ \vdots & \ddots & \vdots \\ A(1, j, n) & \cdots & A(i, j, n) \end{pmatrix}, \quad (3)$$

Interesting parameters are the mean value of grey level of the ij th matrix element in the series of N images $\mu(i, j)$ and the standard deviation of grey level of the ij th matrix element in the series of N images $\sigma(i, j)$:

$$\mu(i, j) = \frac{1}{N} \sum_{n=1}^N A(i, j, n), \quad (4)$$

$$\sigma(i, j) = \sqrt{\frac{1}{N-1} \sum_{n=1}^N [A(i, j, n) - \mu(i, j)]^2}, \quad (5)$$

Results of functions $\mu(i, j)$ and $\sigma(i, j)$ are best presented as contour diagrams in matrix form:

$$\mu(i, j) = \begin{pmatrix} \mu(1, 1) & \cdots & \mu(i, 1) \\ \mu(1, 2) & \cdots & \mu(i, 2) \\ \vdots & \ddots & \vdots \\ \mu(1, j) & \cdots & \mu(i, j) \end{pmatrix}, \quad (6)$$

$$\sigma(i, j) = \begin{pmatrix} \sigma(1, 1) & \cdots & \sigma(i, 1) \\ \sigma(1, 2) & \cdots & \sigma(i, 2) \\ \vdots & \ddots & \vdots \\ \sigma(1, j) & \cdots & \sigma(i, j) \end{pmatrix}. \quad (7)$$

Convergence of the mean value and the standard deviation of grey level was studied to determine the minimum number of images that need to be included in the post processing.

It can be seen that the mean value and standard deviation of grey level in the images do not change significantly when taking in account more than 30 images (Fig. 9). The uncertainty level of less than 1% for the mean value and less than 1.5% for the standard deviation was estimated for the case with 50 images.

Contour diagrams of mean value of gray level μ and standard deviation σ of gray level for cavitation numbers 2.0, 2.3 and 2.5, incidence angle 5° , low and high water gas content and constant upstream velocity 13 m/s for CLE, ALE15 and ALE25 are presented in Figs. 10–15.

The flow is from left to right. The left images show the distribution of mean value (scaled to 0—black, 250—white) while the right ones represent the distribution of standard deviation (scaled to 0—white, 50—black). The upper two images show the top view while the bottom two show the side view.

It can be seen from Figs. 10–12 that the volume of cavitation structure grows when cavitation number decreases (contour diagrams of the mean value of grey level). By decreasing

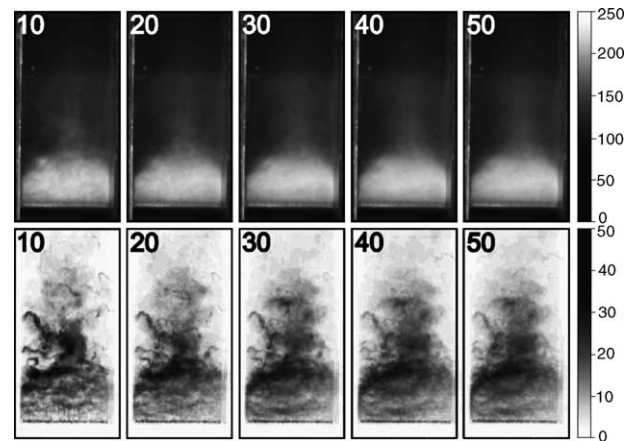


Fig. 9. Convergence test for mean value (upper images) and standard deviation (lower images) of grey level (top view). It can be seen that almost no change in the mean value of gray level or in the standard deviation of gray level can be seen after considering more than 30 images.

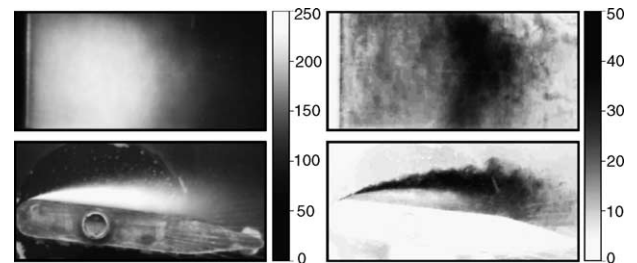


Fig. 10. Mean value and standard deviation of gray level distribution for CLE hydrofoil; $\sigma = 2.0$, low gas content = $14 \text{ mg}_g/\text{l}_w$. Observing the side view we can see that the maximum of standard deviation is far away from the surface of the hydrofoil. The larger distance contributes to lower damage of the surface (observing Fig. 18).

the cavitation number the zone of cavitation cloud separation (in the diagrams characterised by the maximum of standard deviation) moves along the hydrofoil but also away from the hydrofoil surface.

While the diagrams of the mean value of grey level do not show any unusual features, the contour diagrams of the

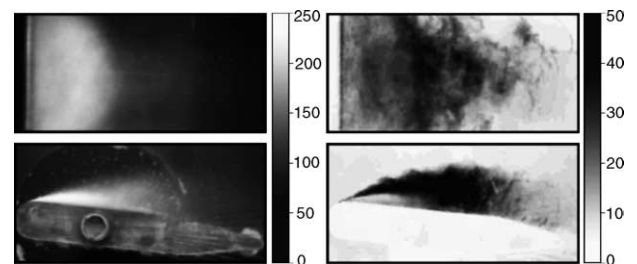


Fig. 11. Mean value and standard deviation of gray level distribution for CLE hydrofoil; $\sigma = 2.3$, low gas content = $13.8 \text{ mg}_g/\text{l}_w$. Side view distribution of standard deviation reveals that the position of the maximum is closer to the surface. It also shows a significant region with higher values of standard deviation, which suggests highly dynamical behaviour of cavitation in this region.

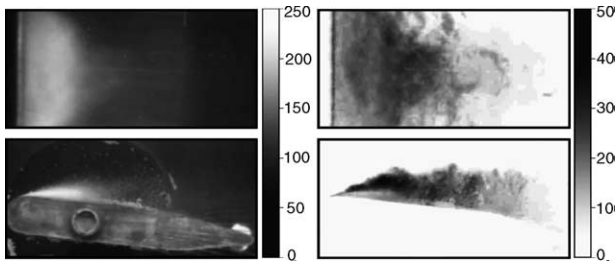


Fig. 12. Mean value and standard deviation of gray level distribution for CLE hydrofoil; $\sigma = 2.5$, low gas content = $14 \text{ mg}_g/\text{l}_w$. The standard deviation of the gray level (both side and top view) is smaller than in Fig. 11, hence we can expect less damage at the surface.

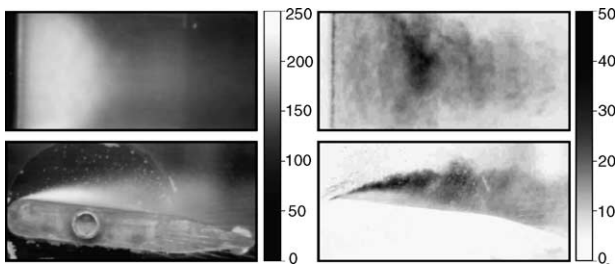


Fig. 13. Mean value and standard deviation of gray level distribution for CLE hydrofoil; $\sigma = 2.3$, high gas content = $48.9 \text{ mg}_g/\text{l}_w$. We can see that the cavitation grows when the gas content is increased. Also, the lower values of standard deviation suggest less dynamical behaviour.

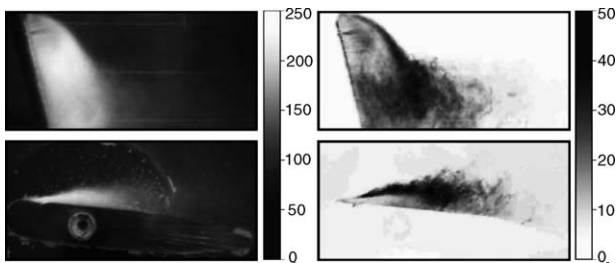


Fig. 14. Mean value and standard deviation of gray level distribution for ALE15 hydrofoil; $\sigma = 2.3$, low gas content = $14.5 \text{ mg}_g/\text{l}_w$. Looking the top view distributions we can see that the maximum of standard deviation is in the region close to the front wall (where the hydrofoil is the shortest), which relates very well to the region where we have dynamical cavitation (cloud separation, observing Fig. 6).

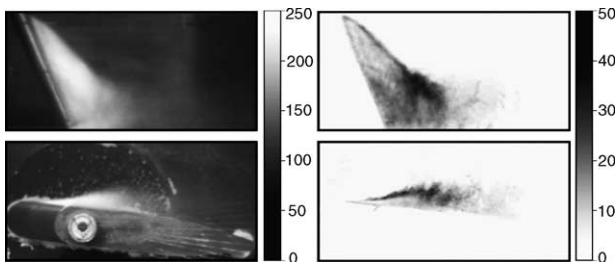


Fig. 15. Mean value and standard deviation of gray level distribution for ALE25 hydrofoil; $\sigma = 2.3$, low gas content = $14.7 \text{ mg}_g/\text{l}_w$. The distribution of standard deviation suggests that the region of where cavitation cloud separation occurs is even more specific (concentrated in the region near the front wall) than in case with ALE15 hydrofoil Fig. 14.

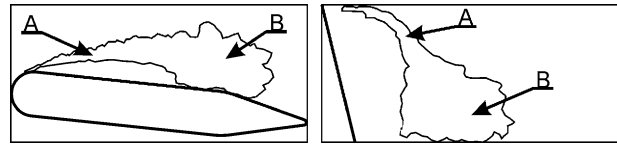


Fig. 16. Schematically presented distribution of the standard deviation distribution for the side (left) and top view (right). The source of the higher value of standard deviation in region B is cavitation cloud separation.

standard deviation of the grey level need to be explained in more detail. Side view diagrams show a significant thin region of higher standard deviation (region A in Fig. 16). The cause for the higher value of standard deviation is not the cavitation cloud separation (region B in Fig. 16) but the small oscillations in the volume of the attached (quasi steady) part of the cavitation. The same phenomenon can be seen in the top view images for the cases with asymmetric hydrofoil. At the back wall of the channel (where the hydrofoil is the longest) a thin region of higher value of the standard deviation at the end of the attached (quasi steady) cavitation can be observed (region A in Fig. 16).

The gas content influences the cavitation structure in two ways. It can be seen that for the high gas content (Fig. 13) the position of the maximum value of standard deviation of gray level is not as specific as in the case of low gas content (Fig. 11). Also, the maximum value is higher for the case of low gas content. The gas content also influences the volume of the cavitation structures. It can be seen that the average cavitation structure is bigger in the case of high gas content, although all other parameters (flow velocity, cavitation number and incidence angle) were the same (diagrams of mean gray value in Figs. 11 and 13).

The cases with asymmetric hydrofoils (ALE15 and ALE25) show obvious 3D asymmetric cavitation structures. By observing the top view contour diagrams of standard deviation (Figs. 14 and 15) we see that the dynamic cavitation phenomenon (separation of cavitation clouds, here characterised by a higher value of standard deviation) occurs only in a region close to the front wall of the cavitation tunnel (where the hydrofoil length is the smallest).

The cavitation image post-processing can serve as a tool to distinguish between steady and unsteady parts of cavitation. The standard deviation maximum (the B type in Fig. 16) is a consequence of highly unsteady cavitation behaviour, which is believed to be the main cause for most of the problems that originate from cavitating flow, also for the cavitation erosion.

6. Pit-count erosion evaluation method

The intensity of cavitation erosion was determined by the pit-count method. The method is based on the assumption that the area of pitted surface and the number of pits that are created by bubble implosions (micro-jet impacts) in a certain time of exposure to cavitating flow give a quantitative measure of the intensity of cavitation erosion.

The pit-count software developed at the Laboratory for Turbomachinery and Fluid Power determines the pits from the darker regions in an image, while the brighter area is assumed to be undamaged surface (a detailed description of optical 2D analyses of a pitted surface can be found in [14]).

Surface image is reconstructed by using a circular structuring element. It has been determined that a circularly shaped structural element 8 pixels (about $16\ \mu\text{m}$) in diameter gives the most plausible results.

A problem that has to be considered is the possibility of overlapping of the pits. Pit clusters are created by chance during longer tests, by collapse of a group of bubbles or by rebounds of a single bubble.

The principle that is used for pit separation is that a single pit cannot form a concave shape. Hence, a concavely shaped dark region is divided into a number of individual objects each having a convex shape. The separated objects are then enlarged to fill out the original object size. If an image object is caused by overlapping pits it is possible that one pixel is shared by two or more pits (Fig. 17).

The pit-count method gives a distribution of the number and the area of the pits and consequently, the distribution of the magnitude of cavitation erosion on the surface.

The distributions of magnitude of cavitation erosion on the surfaces of the hydrofoils for parameters given in Table 1 are presented. A sufficient number of pits was obtained after the hydrofoil was exposed to cavitating flow for a period of 1 h. The exposure time was the same for all cases.

Each contour diagram is a result of an interpolation of pit-count measurements at approximately 925 positions on the hydrofoil surface.

The flow is from bottom to top. The results of surface damage for the low gas content ($<15\ \text{mg}_g/\text{l}_w$) are scaled to 0% surface damage—white and 10% surface damage—black. In the case of high gas content ($>45\ \text{mg}_g/\text{l}_w$), the scale is 0% surface damage—white and 2% surface damage—black. The value of eroded surface (ES) represents the part of the whole surface that is damaged (covered by pits).

It can be seen that the ES maximum occurs at cavitation number 2.3 in the case of the CLE hydrofoil (Fig. 18). The reason for this is that the dynamic behaviour of cavitation is not strong enough to cause more damage to the surface in the case of cavitation number 2.5. On the other hand, in the case with cavitation number 2.0, the cavitation moves further away from the leading edge of the hydrofoil (cavitation cloud

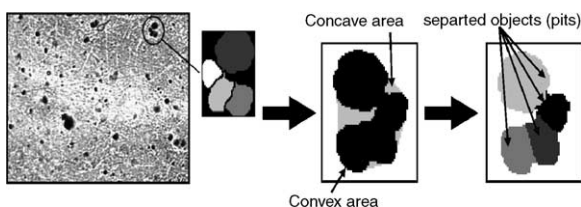


Fig. 17. Detection of pits on the surface by the pit-count method. The program recognizes the darker regions as damaged surfaces. It can also distinguish several pits that are overlapping.

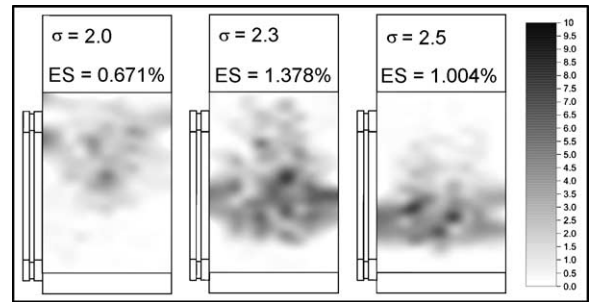


Fig. 18. Pit distribution for CLE hydrofoil, low gas content $<15\ \text{mg}_g/\text{l}_w$. The maximum of damage moves away from the leading edge as cavitation number is decreasing. The position of the maximum of damage corresponds to position of cavitation cloud separation, characterised by higher value of standard deviation (Figs. 10–12).

separation occurs at the end and also behind the copper foil; Fig. 10) and the cloud implosions occur further away from the surface (amplitude of the emitted shock wave is decreased by the distance until it reaches the surface of the hydrofoil) contribute to the smaller damage of the copper coated surface of the hydrofoil.

As expected the water gas content plays a major role in the process of cavitation erosion. The surface sustains up to 50 times less damage in cases with high gas content than in cases with low gas content (Figs. 18 and 19). The reason probably lies in the fact that presence of gas in water attenuates the pressure wave emitted by the bubble cloud implosion (Fig. 1). The bubbles near the surface do not begin to oscillate and the micro-jet phenomenon that causes the surface erosion does not occur.

The cavitation structures in the cases with asymmetric hydrofoil (ALE15 and ALE25) show dynamic cavitation behaviour only in the region near the front wall (where the hydrofoil length is the smallest) (Figs. 14 and 15). As expected the surface damage corresponds to the position of the higher value of standard deviation of gray level (comparing Figs. 14 and 15 with Figs. 20 and 21). The results confirm the hypothesis that the cavitation erosion is conditioned by the dynamic behaviour of cavitation (cavitation cloud separation).

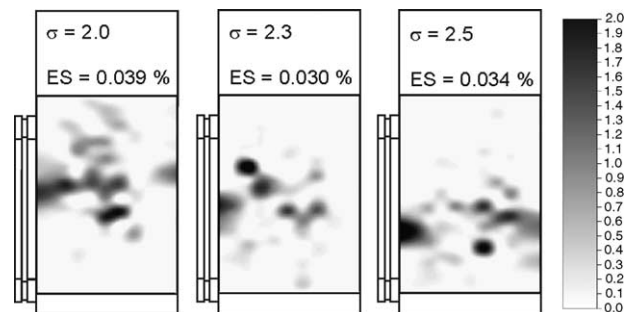


Fig. 19. Pit distribution for CLE hydrofoil, high gas content $>45\ \text{mg}_g/\text{l}_w$. An obvious influence of gas content can be seen. The surface sustained up to 50 times less damage when high gas content was used (comparing data in Figs. 18 and 19).

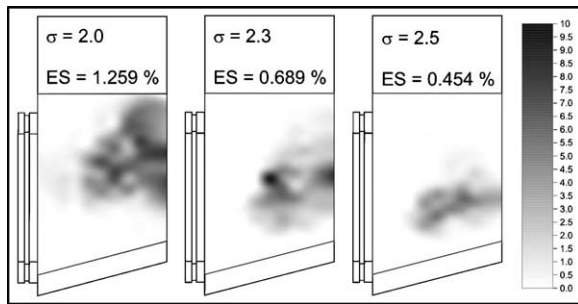


Fig. 20. Pit distribution for ALE15 hydrofoil, low gas content $< 15 \text{ mg}_g/\text{l}_w$. Results show that the cloud separation is a needed condition for cavitation damage. The hydrofoils were significantly damaged only in the region where cavitation cloud separation occurs.

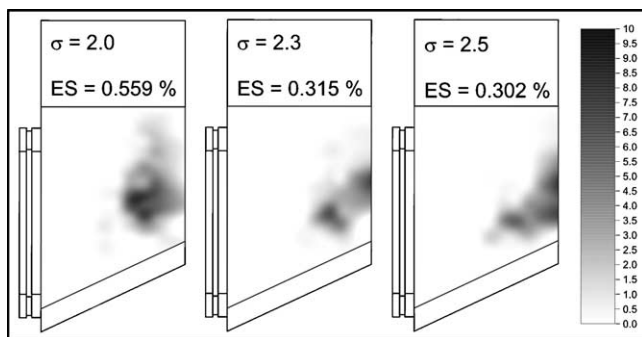


Fig. 21. Pit distribution for ALE25 hydrofoil, low gas content $< 15 \text{ mg}_g/\text{l}_w$. The relation between cavitation cloud shedding and cavitation damage is even more obvious in the case of ALE25 hydrofoil (in comparison to the ALE15 hydrofoil; Fig. 20).

The ES value increases with decreasing cavitation number for the ALE15 and ALE25 hydrofoils. The reason lies in different flow pattern. The length of the cavitation structure does not exceed the length of the copper foil (even in the case with cavitation number 2.0), hence, the cavitation cloud separation always occurs above the copper foil. Moreover, the distance of cloud implosion from the surface of the hydrofoil remains approximately constant and does not increase with decreasing cavitation number as in the case for the CLE hydrofoil.

7. Conclusions

A study of visually observable and erosion effects of cavitation was presented. Three different hydrofoil configurations were used and 12 different tests were conducted.

It was found that the value of standard deviation of grey level could be used as the parameter for describing the unsteadiness of cavitation.

An obvious correlation between cavitation structures and cavitation erosion was found. The position and distribution of pits on the copper coated surface correlates to the distribution of the standard deviation of grey level.

A hypothesis that the cavitation erosion is conditioned by the dynamic behaviour of cavitation (cavitation cloud separation) was successfully confirmed.

References

- [1] L. Rayleigh, On the pressure developed in a liquid during the collapse of a spherical cavity, *Philos. Mag.* 34 (1917) 94–98.
- [2] T.G. Leighton, *The Acoustic Bubble*, Academic Press, London, 1997.
- [3] T.B. Benjamin, A.T. Ellis, The collapse of cavitation bubbles and the pressures thereby produced against solid boundaries, *Philos. Trans. R. Soc. London* 260 (1966) 221–240.
- [4] M.S. Plesset, R.B. Chapman, Collapse of an initially spherical vapour cavity in the neighbourhood of a solid boundary, *J. Fluid Mech.* 47 (1971) 283–290.
- [5] W. Lauterborn, H. Bolle, Experimental investigations of cavitation-bubble collapse in the neighbourhood of a solid boundary, *J. Fluid Mech.* 72 (1975) 391–399.
- [6] N.K. Bourne, J.E. Field, Shock-induced collapse of single cavities in liquids, *J. Fluid Mech.* 244 (1992) 225–240.
- [7] K.A. Mørch, *Erosion*, Academic Press, London, 1979.
- [8] R.P. Tong, W.P. Schiffers, J.S. Shaw, J.R. Blake, D.C. Emmony, The role of splashing in the collapse of the laser-generated cavity near a rigid boundary, *J. Fluid Mech.* 380 (1999) 339–361.
- [9] R. Böhm, Erfassung und hydrodynamische beeinflussung fortgeschrittener kavitationszustände und ihrer aggressivität, Ph.D. thesis, Technische Universität Darmstadt, Darmstadt, 1998.
- [10] M. Hofmann, Ein beitrag zur vermindern des erosiven potentials kavitierender stömungen, Ph.D. thesis, Technische Universität Darmstadt, Darmstadt, 2001.
- [11] H. Lohrborg, Messung und aktive kontrolle der erosiven aggressivität der kavitation in turbomaschinen, Ph.D. thesis, Technische Universität Darmstadt, Darmstadt, 2001.
- [12] T.G. Leighton, M. Farhat, J.E. Field, F. Avellan, Cavitation luminescence from flow over a hydrofoil in a cavitation tunnel, *J. Fluid Mech.* 480 (2003) 43–60.
- [13] J.L. Reboud, R. Fortes-Patella, A. Archer, Analysis of damaged surfaces. Part I. Cavitation mark measurements by 3D laser profilometry, in: *Proceedings of the Third ASME/JSME Joint Fluids Engineering Conference*, San Francisco, CA, 1999.
- [14] H. Lohrborg, M. Hofmann, G. Ludwig, B. Stoffel, Analysis of damaged surfaces. Part II. pit counting by 2D optical techniques, in: *Proceedings of the Third ASME/JSME Joint Fluids Engineering Conference*, San Francisco, CA, 1999.
- [15] P. Bourdon, R. Simoneau, J.M. Dorey, Accelerometer and pitcount detection of cavitation erosion on a laboratory jet and a large francis turbine, in: *Proceedings of the XVII IAHR Symposium*, Beijing, 1994.
- [16] Y. Ito, R. Oba, Comparison between four practical methods to detect the erosive area in cavitating flows, in: *Proceedings of the XVII IAHR Symposium*, Beijing, 1994.
- [17] R. Simoneau, Cavitation pit counting and steady state erosion rate, in: *Proceedings of the International Symposium on Cavitation Cav'95*, Deauville, 1995.
- [18] S. Lavigne, A. Retailleau, J. Woillez, Measurement of the aggressivity of erosive cavitating flows by a technique of pits analysis. Application to a method of prediction of erosion, in: *Proceedings of the International Symposium on Cavitation Cav'95*, Deauville, 1995.
- [19] B. Bachert, G. Ludwig, B. Stoffel, B. Sirok, M. Novak, Experimental investigations concerning erosive aggressiveness of cavitation in a radial test pump with the aid of adhesive copper films, in: *Proceedings of the Fifth International Symposium on Cavitation*, Osaka, Japan, 2003.

- [20] X. Escaler, M. Farhat, F. Avellan, E. Egusquiza, Cavitation erosion tests on a 2D hydrofoil using a surface-mounted obstacles, *Wear* 254 (2003) 441–449 (Elsevier).
- [21] F. Pereira, F. Avellan, P. Dupont, Prediction of cavitation erosion: an energy approach, *J. Fluids Eng.* (1998) (The American Society of Mechanical Engineers).
- [22] M. Dular, B. Sirok, M. Novak, M. Hocevar, B. Stoffel, G. Ludwig, Development of the cavitation erosion prediction method in hydraulic machines, in: *Proceedings of the 15th International Congress on Condition Monitoring and Diagnostic Engineering Management (COMADEM 2002)*, Birmingham, UK, 2–4 September, 2002.
- [23] B. Sirok, M. Dular, M. Novak, M. Hocevar, B. Stoffel, G. Ludwig, B. Bachert, The Influence of cavitation structures on the erosion of a symmetrical hydrofoil in a cavitation tunnel, *J. Mech. Eng.* 48 (7) (2002) 368–378.
- [24] Y. Iwai, S. Li, Cavitation erosion in waters having different surface tensions, *Wear* 254 (2003) 1–9 (Elsevier).